

¹ Masters Thesis: The Evolution of Fault Slip Surfaces with
² Cumulative Displacement

³ Kelian Dascher-Cousineau

⁴ February 27, 2017

⁵ **Abstract**

Fault slip surface roughness determines fault strength, friction and dynamic fault processes. Wear models and field observations suggest that roughness decreases with cumulative displacement. However, measurements have yet to isolate the effect of displacement from other possible controls, such as lithology or tectonic setting. We present an unprecedentedly large fault surface dataset collected in and around the San-Rafael Desert, S.E. Utah, United States. In the study area, faults accommodated regional extension at shallow 1 to 3 km depth and are hosted in the massive, well sorted, high porosity Navajo and Entrada sandstones. Existing detailed stratigraphic throw profile provide a maximum constraint for displacement. Where cross-sectional exposure is good, we measure exact displacement imparted on slip surfaces using offset in marker horizons. Thereby, we isolate for the effect of displacement during the embryonic stages of faulting (0 to 60 m in displacement). Our field observations indicate a clear compositional and morphological progression from isolated joints or deformation bands towards smooth, continuous and mirror-like fault slip surfaces with increasing displacement. To quantify these observations, slip surfaces were scanned with a white light interferometer, a laser scanner and a ground based Lidar. Together these instruments resolve more than eight decades of spatial bandwidth (from less than μm 's to m's in scale). Preliminary results indicate that roughness decreases with displacement according to a power law. Roughness measurement associated with only maximum constraints on displacements corroborate this result—for a given displacement, minimum roughness is bounded by the later smoothing trend. In addition, we find that the maximum roughness is fixed—bounded a by a primordial roughness corresponding to that of joints surfaces and deformation band edges. Our results build towards a coherent model of fault wear robust to ambiguities associated to displacement estimates, spatial scaling and geological context.

³⁰ *Will have to include relationship to white light data, modelling results/interp*

³¹ **Contribution of Authors**

³² **1 Introduction**

Faults are a characteristic feature of the Earth's brittle crust. Fluid flow, seismicity and crustal mineralization are just few systems upon which faults act as major controls (Sibson, 1977). In spite of their importance, some aspects of faults and their underlying processes remain poorly understood. How strong is a fault? How do faults mature? Are small faults mechanically different to large faults? Fault geometry has been shown to be a key parameter controlling the mechanical behavior and evolution of faults (e.g. Lay et al., 1982; Aki, 1984; Power et al. 1988; Chester and Chester, 2000), but these questions are not yet fully answered.

Slip on a fault occurs on discrete slip surfaces in fault zones (Davatzes and Aydin, 2005). These surfaces are not planar; they are rough. Roughness is observable at all scales (Scholtz and Aviles, 1986; Candela et al., 2012). Slickenlines, corrugations, mullions and jogs are all surface features that can be seen at different length scales (Sagy and Brodsky, 2009). Field studies have found common characteristics in the topography of fault surfaces. These can be summarized as follows: 1) Fault surfaces appear to be well defined by large fractal domains, wherein 2) faults are smoother at larger length scales (Scholtz and Aviles, 1986; Candela et al., 2012), 3) rougher in the slip perpendicular direction than in the slip parallel direction (Lee and Bruhn, 1996), and 4) slip surfaces are smoother with cumulative displacement (Sagy et al., 2007). Fault roughness has been demonstrated to be critical in determining the strength (Chester and Chester, 2000, Brodsky et al., 2016), triggering (Parsons, 2008), dynamic properties (Candela et al., 2011; Dunham et al., 2011), spatial distribution (Parson, 2008) and failure recurrence of faults (Stirling et al., 1996). It is increasingly evident that roughness is a fingerprint of fundamental features of the faulting process (Brodsky et al., 2016). In accordance, incorporating more complex sources geometries has become a more frequent practice in dynamic earthquake rupture modelling (Shi and Day, 2013; Dunham et al., 2011).

Changes in roughness, as determined by cumulative displacement (Sagy et al, 2007; Brodsky et al, 2011), imply faults mature. Fundamental differences between immature and mature fault have far-reaching implications. Fixed source parameter scaling of earthquakes is a pillar of earthquake seismology. However, analysis of seismic signals of immature faults vs. mature faults suggest that scaling is sensitive to cumulative displacement. This observation leads to an interpretation of fundamental differences in earthquake populations. Specifically fault maturation would undermine the applicability of a constant magnitude scaling. Evolving mechanical properties such as fault friction and static strength—both associated to fault roughness—would imply that immature and mature faults belong to distinct populations with distinct scaling. (Harrington and Brodsky, 2011)

While there has been significant progress in understanding the role of roughness in the faulting process, how and why fault surfaces change is still unclear (e.g. Candela et al., 2011; Dunham et al., 2011; Brodsky et al., 2016). Sagy et al. (2007) noted a systematic decrease in roughness of ‘mature’, large displacement faults compared to ‘immature’ faults with low displacements. Similar results have since been observed along reactivated joints, in laboratory experiments (Davidesko et al., 2014), and in compilations of fault roughness analysis (Brodsky et al., 2011; Candela et al., 2012). These studies all attribute the decrease in roughness to wear at the fault interface. However, these data show only weak correlations between fault roughness and cumulative displacement. Indeed, relating roughness and cumulative displacement is not trivial. Fault surfaces in exhumed faults are rarely well preserved. Furthermore, obtaining well-constrained displacement estimates is contingent on the presence of precise and accurate kinematic indicators. Combining observations over a broad range of displacements is challenging. Consequently, it is unclear whether trends observed in compilations of roughness measurements from multiple faults are directly attributable to displacement or a combination other geological factors. For instance, while comparing fault surfaces from geologically diverse datasets, variations in lithology, faulting mechanism, temperature and depth may all be introducing further systematic variations.

Additionally, the evolution of roughness represents a novel insight into the architecture of a fault zone. The geometry of the fault surface modulates the architecture of the whole fault zone (Mitchell and Faulkner, 2009). Changes in roughness require interaction between the slip surfaces and its direct surrounding (fault core), resulting in the formation of fault rock (Power and Tullis, 1988). In addition to earthquake mechanics, the architecture of a fault zone, and its corresponding permeability structure, is very important for hydrocarbon exploration (Shipton and Cowie, 2003). However, because the change in roughness by wear is poorly understood,

90 the equivalent production of wear material, the fault rock, is also poorly understood. Fault
91 rock thickness growth with displacement is documented (Sholtz, 1987), but variability is such
92 that even order of magnitude estimates of thickness for a given displacement are unavailable.

93 In this study, we report on how fault surfaces change. In line with previous studies, I hy-
94 pothesize that faults smooth with displacement and that wear is a dominant mechanism in the
95 evolution of fault surfaces with cumulative displacement. We measure the surface roughness
96 of natural fault surfaces with varying displacements to confirm and better quantify the role of
97 cumulative displacement on fault roughness. Field work in Southern Utah was conducted to
98 collect scans of pristine fault surfaces with terrestrial laser scanners and hand-samples for labo-
99 ratory high resolution scans. Fault roughness is then be quantified and related to corresponding
100 displacement. A robust quantitative correlation between roughness and cumulative displace-
101 ment enables the parameterization of semi-analytical wear model for fault surfaces. Moreover,
102 based on my results, I produce an external estimate of fault rock production in the fault zone.

103 1.1 Fault Roughness

104 The deviation from planarity formally defines roughness (Brown and Scholz, 1985). Pioneering
105 studies used contact profilometers to measure the roughness of fault surfaces (Scholz and Aviles,
106 1986; Power and Tullis, 1991. Combined with surface profiles of large scale continental faults,
107 faults were found to have a remarkably broad fractal band ranging over 10 orders of magni-
108 tude—from 10^{-5} to $10^5 m$ (Scholz and Aviles, 1986). Over these length scales, fractal scaling is
109 said to be statistically self-affine. A statistically self-affine profile along x with heights $h(x)$, is
110 invariant under the affine transformation:

$$\left\{ \begin{array}{l} x \rightarrow \lambda x \\ h \rightarrow \mu h \end{array} \right\} \quad (1)$$

111 This relation therefore implies an exponential relation between the scaling, λ (along x), and
112 μ (along h) such that:

$$\mu = \lambda^\varsigma \quad (2)$$

113 Where ς is a constant named the Hurst exponent. Note that self-similarity, is an instance
114 of self-affinity where the Hurst exponent is 1 (Schmittbulh et al., 1993). Developments in laser
115 scanner technology over the past decade, particularly terrestrial laser scanners, allowed surfaces
116 to be characterized by calculating the Hurst exponent from thousands of cross sectional profiles
117 through a fault surface (e.g. Candela et al., 2012). Studies of natural mode I crack surfaces have
118 observed self-affinity with a Hurst exponent of ~ 0.8 at all scales of observation (Scholtz, 1985).
119 Shear, or mode II cracks (i.e. faults) are different. They are anisotropic—the Hurst exponent
120 parallel to shear (~ 0.6) is smaller than that in the shear-perpendicular direction (~ 0.8) (Lee
121 and Bruhn, 1996).

122 Another parameter is required to fully describe surface roughness. While the Hurst ex-
123 ponent describes the scaling behavior of the roughness it does not define the magnitude of
124 the roughness. The pre-factor defines the amplitude of the scaling law (Candela et al., 2009).
125 The pre-factor is subject to significant variation. Overall, observations show that fault surfaces
126 have distinctly smoother profiles along slip direction than perpendicular to slip (Lee and Bruhn,
127 1996). Many methods exist to quantify roughness scaling, possibly most intuitive of which is
128 the Root Mean Squared (RMS) as a function of scale. For a profile of length L with a point
129 spacing of Δx with deviation h from the best fit line, the RMS for a given scale s is defined as
130 follows:

$$RMS(s) = \sqrt{\frac{\Delta x}{L} \sum_{i=1}^{L/\Delta x} h_i^2} \quad (3)$$

The *RMS* roughness of a fault or fracture exhibits power-law scaling with segment length. A self-affine profile should therefore plot as a straight line on a log-log plot of the *RMS* as a function of the segment length with a slope equivalent to the Hurst exponent. (Schmittbuhl et al., 1993) The power spectrum of a surface profile has been shown to yield more robust roughness metrics (Schmittbuhl et al., 1993; Candela et al., 2009). For a set of discretely sampled points, the power spectrum of a profiles is the result of a Fast Fourier Transform (FFT). The spectrum defines the surface profile as superposition of sinusoidal profiles. In the frequency domain, rougher profiles will have correspondingly higher amplitudes, or power. The power spectrum, $P(k)$, of a self-affine profile (again in log-log space) defines a line as follows:

$$P(k) = Ck^{(-1-2\zeta)} \quad (4)$$

Where k is the frequency and C is the pre-factor (Candela et al., 2009).

1.2 Wear

1.3 The evolution of slip surfaces with displacement

talk about deformation in sandstones, e.g. aydin, fossen etc.

In this project, I hope to address how slip surfaces change. Many processes could cause the slip surface to change. In fact, the cause of change to the slip surface is not uniquely recorded by the roughness. Fundamentally, a fault surface can only change according to the following mechanisms:

Addition of material

Redefinition of the slip surface by fracture

Removal of material

I have hypothesized that the change in surface roughness is the result of wear—an instance of removal of material. As fault blocks slide past each other, frictional wear is an inevitable process. Layers of comminuted fault rock are direct evidence of this process (Power and Tuillis 1988). Wear is the subject of a vast field of research, particularly in engineering and tribology due to interest in lubricating and manufacturing machine parts for longevity (Meng and Ludema, 1995). Here, I outline only basic wear mechanics (i.e. Archard, 1953). Wear is formally defined as frictionally induced volume removal from surfaces in sliding contact. The wear rate, the amount of wear per unit distance is broadly related to the real area of contact and loading. When two surfaces are put in direct contact, the real area of contact is much smaller than the nominal surface areas because the load is supported at microscopic protrusions from a surface, called asperities. Remote loading normal to the surface causes local stresses and associated deformations at contact points. Note that as the load is increased, deformation of large asperities causes new asperities to come in contact. In its simplest form, wear rate defined as:

$$W \propto \frac{P}{a} \quad (5)$$

Where W is the wear rate, P is the remote load and a is a mean measure of the dimensions of the asperities in contact during sliding. The relation has been shown to be reasonably robust

in experimentation for most materials. In further detail, the size, distribution and duration of contact areas, as well as the shape of the worn particles, control the general behavior of wear. Note that material properties are implicitly buried in a probability factor—the probability of a collision of asperities to lead to removal of material (Archard, 1953). If and how wear affect the geometry of a fault slip surface remains unclear. Both field and laboratory experiment show that wear is scale dependent, such that asperities are worn down at different rates according to their typical dimensions. Asperities at longer characteristic wavelengths and larger amplitudes wear down faster, on average, than those with small wave lengths and small amplitudes. These observations correspond to both a downward translation and clockwise rotation of the self-affine scaling in the power spectrum. The exact mechanism causing this behavior is unclear. Davidesko et al., 2014 suggest that dilation during displacement on a fault ‘shelters’ smaller, shorter wavelength, asperities and therefore wears down large, long wavelength asperities. In this study, I hope to be able to relate changes in the slip surface geometry to wear processes. Specifically, empirically identifying and determining the rate of wear as expressed in the slip surface would be of particular interest. A potential caveat to the simple wear models (i.e. Archard, 1953) is the sensitivity of fault rock to sliding velocity and the presence of lubricant (e.g. pseudotachylyte, amorphous silica gel and gouge). Moreover, the stresses imparted by a propagating fault rupture front are mechanically distinct from those related to rubbing surfaces. Such a distinction may also drastically alter the relation between wear material and the slip surface (Sibson, 1977). Since Archard (1953), models of wear tend to diverge in their results, assumptions and by association, their applicability (Meng and Ludema, 1995). For the purpose of this study, the fractal nature of fault surfaces is important to reconcile with a model of wear. What is the scaling behavior of wear? Fractal surfaces are difficult to integrate into the pre-existing framework of wear processes. Specifically, defining the real area of contact, corresponding deformation and, by association, the scale dependence of wear is non-trivial (e.g. Persson, 2001; Jackson and Streator, 2006).

2 Geology

All data presented in this study was collected in the San-Rafael Desert, Utah (see figure 1). The San Rafael Desert hosts a sequence of gently dipping marine and sub-areal sedimentary rocks deposited from the Pennsylvanian to the Jurassic (see Figure 2). The San Rafael Desert is part of the San Rafael Swell, a monocline that formed when these sediments were uplifted as a passive drape fold above a reactivated basement reverse fault during the Late Cretaceous Laramide Orogeny (Kelly, 1955; Vrolijk et al., 2005). The swell is part of the broader Colorado Plateau (Kelly, 1955). Networks of joints and normal faults associated to further Laramide activity cross-cut sedimentary sequence accommodating North-South extension (Aydin and Johnson, 1978; Vrolijk et al., 2005). Within the San Rafael Swell we focus the following field locations: 1) the Chimney Rock Fault Array, 2) the Big Hole fault and 3) a network of deformation bands in the Entrada formation near Goblin Valley State Park. Advantages of theses field locations are manifold. First, the nearly pure quartzite lithology, extensional tectonic regime, depth (2-4 km or 40-80 MPa), temperature (estimates range from 45-90 °C) of activity, and faulting mechanism are all relatively consistent (Vrolijk et al., 2005). Consistency in these parameters is key to isolating the effect of displacement on the fault roughness. Moreover, both field locations exhibit well preserved fault surfaces that are exposed and accessible (see Figure 3). The Chimney Rock fault array is an orthorhombic set of faults that crops out at the northern end of the San Rafael Swell (Krantz, 1989, Davatzes et al., 2003). Two pairs of oppositely dipping normal faults crop out at the surface with preserved fault scarps. WNW-striking faults are interpreted to have formed by shear reactivation of joints, whereas ENE-striking faults initially formed from deformation bands (Davatzes, 2003). Exposure is very good, faults are abundant and have

well preserved fault surfaces (Vrolijk et al., 2005). The Chimney fault array has studied to better understand of fault geometry (Shipton and Cowie, 2001; Shipton and Cowie, 2003), permeability (Shipton et al., 2002) and kinematics (Krantz, 1986; Krantz, 1989; Maerten et al., 2001; Davatzes et al., 2003) . As a result, detailed maps of the fault array have been produced (e.g. Maerten et al., 2001) . In addition, by using measurements of the separation between footwall and hanging wall cutoffs of sedimentary horizons, entire displacement profiles have been measured for faults with a wide range of displacements (Cowie and Shipton, 1998; Maerten et al., 2001; Shipton and Cowie 2001; Shipton and Cowie, 2003). The Big Hole fault is located just to the South-East of the Chimney Rock Fault Array. While not explicitly part of the fault array, the Big Hole fault shares a nearly identical geological setting. The Big Hole fault has been extensively studied in detail as an analog to hydrocarbon reservoir-scale faults. Displacements on the exposed fault range from 8 m to 39 m. (Shipton and Cowie, 2001; Shipton and Cowie, 2003) Large networks of deformation band faults outcrop near Goblin Valley State Park on the southeastern margin of the San-Rafael Swell (Aydin and Johnson, 1978). Deformation bands are the result of concentrated shear deformation on narrow centimeter thick bands (Aydin and Johnson, 1978; Davatzes et al., 2003). Collapsing pore space accommodates this deformation. Deformation bands are interpreted as the embryonic stages of fault development (Fossen and Hesthammer, 1998; Fossen et al., 2007). Because deformation bands dramatically alter the local permeability structure, Goblin Valley has been extensively studied in light of fault nucleation and the implications for hydrocarbon circulation (e.g. Fossen et al., 2005; Tobari and Fossen 2009). At Goblin valley, arrays of deformation bands anastomose—outcropping as centimeter- to meter-sized slabs. These are often bounded by discrete slip surfaces with well-preserved striations — i.e. roughness (Aydin and Johnson, 1978). Offsets in sedimentary beds have allowed previous studies to obtain detailed displacement measurements (e.g. Schultz and Fossen 2002). Together, these field locations offer the chance to survey well-preserved fault surfaces that have hosted displacements from embryonic stages to 30 m of displacement. Moreover, novel to this study, we are able to survey multiple expressions of a single fault’s surface with various displacements according the displacement profile of the fault.

3 Method

This study focuses on the qualitative and quantitative evolution of fault slip surfaces—both addressing how fault slip surfaces evolve and the implications thereof. The quality of the displacement measurements and the large number of accurate surface scans are fundamental to the quantitative analysis of the data. Field-method and data acquisitions thus reflect these standards.

For the qualitative analysis, we carefully record the characteristics of the fault architecture in the context of fault evolution. Specifically, we are particularly meticulous about 1) identifying cross-cutting relationships which indicate temporal evolution on the on fault, 2) identifying the evolutionary stages in the formation of faults and 3) identifying and characterizing the wear product, or fault rock, produce as faults evolve.

For the quantitative analysis, we collect scans both *in situ* and from hand samples collected in the field. Scans are associated to a constraint on displacement. Moreover, for every scan, the time of day, location, quality, strike and dip of the fault slip surface as well as the rake of the slickenlines are recorded. When possible we record an estimate of the fault rock thickness. Finally, we also record both a plan and cross-sectional view image of the scanned fault surfaces. See appendix for the tabulation of this data. Together, all these measurements and observations should provide the necessary data to robustly explain and quantify the process through which faults mature.

262 **3.1 Scan Data Acquisition**

263 To measure slip surface roughness, we analyses large point clouds scans of real fault surfaces and
264 average the slip parallel and perpendicular spectral and statistical properties across hundreds
265 of profiles. Point clouds must be obtained across a flexible array of instruments to properly
266 capture the fractal scaling behavior (Brown and Scholtz, 1985; Candela et al., 2012). In this
267 study, we use three instruments with complimentary scales of observation. Together, these
268 instruments offer accurate and precise three-dimensional discretization of fault surfaces at over
269 nine decades of length scale.

270 *make a map of each areas with the location of every scan encoded with different symbols*

271 At the largest scales ranging from meters down to millimetres, a light detection and ranging
272 instrument (i.e. LiDAR). We use the LiDAR has been used in many previous studies of fault
273 roughness as it is easily deployable in the field and provides rapid means to collet very large point
274 cloud data set. However, its use is limiting as it requires exceptionally good and, accordingly,
275 rare exposure of fault surfaces that are large enough and fresh enough to not have been degraded
276 by erosion. In this study, we report 5 ??? Lidar Scans (see figure).

277 Instead, the bulk of in situ field measurements were made at intermediate scales ranging
278 from centimeters down to hundreds of microns with the NextEngine 3D laser scanner. The
279 NextEngine laser scanner is accurate down to 100 microns with resolution up to 41 540 points
280 per square centimeter. Note that the NextEngine is a much less cost prohibitive option when
281 compared to the LiDAR yet captures the same characters of the fault surfaces. The laser
282 scanner was benchmarked to a machined-flat granite surface and to a scan of the corona slip
283 surface both to industrial-grade laser scanner as reference. The scanner is not exactly built to
284 be field ready. It requires a power source, low light conditions, a stable surface to sit on, limited
285 dust exposure and must be connected to a computer. Moreover it only allows for a very limited
286 depth of field. To use the scanner in the field, we connected both the laser scanner and laptop
287 to a solar powered, *goal zero*, battery. The scanner was encased and padded in a reinforced
288 cardboard box with its depth exactly equivalent to the optimal depth of field. The set up had
289 the added advantage of being very portable, completely removing sunlight and limiting dust
290 exposure. We report XXX scans using the NextEngine Laser scanner.

291 Finally, hand samples were collected and analyzed with the Zygo blah blah, an optical
292 profilometer enabling accuracy from millimeters down to sub-micron. The Zygo blah blah
293 uses white light interferometry to produce relatively small point-clouds (XXX points) a various
294 magnifications. It does however allow for seamless stitching of scans. Individual and stitched
295 scans using the profilometer where benchmarked to a silicon carbide reference machined flat to
296 XXX meters. All samples where scanned at 20x magnification and stitched together to produce
297 sections roughly XXX by XXX millimeters. In additions, samples where scanned at the lowest
298 magnification to properly bridge the gap up to the laser scanner resolution. We report scans
299 of XXX samples with the white light profilometer, XXX of which were taken from surfaces
300 scanned in the field with the laser scanner.

301 **3.2 Constraining displacement**

302 We associate every scan with a displacement constraint. Field areas where specifically chosen
303 for the exceptional exposure and relatively simple offset markers. For the Chimney Rock Fault
304 Array and Big Hole Fault entire displacement profiles have been measured during previous
305 detailed mapping campaigns (i.e. Maarten shipton). At Iron wash, Horse Creek and Molly's
306 Castle, Atilla Aydin's mapping identified clear offset markers. Base maps for all these areas
307 were georeferenced onto satellite images and used in the field to streamline data acquisition.
308 Where fault exposure was good, we populated the maps with additional measurements using
309 basic tape measure and compass triangulation methods.

310 It is important to recognize that the base maps only report stratigraphic throw or, in some
311 cases, actual offset across *entire* fault zones. In the field we typically observe not one, but
312 many slip surfaces along with very complex networks of deformation bands and sheared joints
313 which partition displacement across many interfaces throughout the fault zone (see figure).
314 In this study, we make a distinction between *offset* across the entire fault and *displacement*
315 across a single fault slip surface. Without good marker horizons and cross-sectional exposure,
316 determining how stratigraphic offset is accommodated across slip surfaces can be ambiguous,
317 and thus requires detailed outcrop mapping (e.g. shipton ???) At Big Hole fault, two large-
318 scale continuous strands of the fault, both accommodating meters of displacement exemplify this
319 mechanism at a larger scale. In accordance, Shipton and Cowie, 2003 report large uncertainty on
320 the partitioning of stratigraphic offset across the two strands. This implies that offset across the
321 entire fault zone is an upper-bound constraint on displacement for a given slip surface. In XXX
322 of XXX fault slip surface measurements, this is the best available constraint on displacement.

323 We were able to reconstruct exact displacement and offset partitioning where cross-sectional
324 in the following specific cases: 1) If cross sectional exposure indicates that there is only a single
325 slip surface; 2) If cross-sectional exposure is good enough to clearly indicate the fault trace, an
326 offset marker (lamella, cross-bedding or lithological contact) and near enough to the slip surface
327 exposure; or 3) if it is unambiguous that one slip surface is accommodating an overwhelming
328 majority of displacement, i.e. it is continuous, it has a layer of fault rock and it distinctly more
329 linear and sharp than any other slip surface in the fault zone.

330 While the latter does not preclude the possibility for displacements to be accommodated on
331 other smaller slip surfaces, for larger displacement faults (more than 10 m of slip), these smaller
332 displacements will not amount to a significant portion of the total slip. In detailed outcrop maps,
333 Shipton showed that the displacement accommodated by small discontinuous slip surfaces was
334 minimal compared that accommodated by an unambiguous large displacement strand, here on
335 after referred to a *principle slip surface* (PSS).

336 Cases where a clear PSS is unambiguously identifiable allowed us to characteristically further
337 criteria for a confident identification of a PSS for the Navajo and Entrada Sanstones as follows:

- 338 • *The PSS is an interface between two displaced fault blocks.* As such juxtaposition of two
339 distinct rock types (e.g. distinct stratigraphic horizons and/or fault rock) by faulting is
340 an unambiguous indicator;
- 341 • *the PSS has a distinctly sharp, continuous, relatively planar morphology in cross section.*
342 A certain panarity must exist to prevent substantial geometric mismatch;
- 343 • *in line with the implicit definition of a fault, the PSS is nearly cohesionless.* Locations
344 identified to be expose section of a PSS inevitably cracked open when sampling across the
345 slip surface—the slip surfaces had no cohesion. Cohesion is typically thought to reinstate
346 by precipitation and healing. We did not observe recovered healing in this study.
- 347 • *the PSS has a vitreous finish;*
- 348 • *The PSS is typically in the center of a damage zone.* Damage is an inevitable conse-
349 quence of displacement and the accompanying mismatch that accumulates. Damage at
350 the field locations in this study is expressed as comminution (e.g. cataclasite and gouge),
351 fragmentation (e.g. breccia, splay joints) and shear deformation (specifically deformation
352 bands).

353 *make a table regarding the different types of displacement constraints*

354 known unknown equation assumptions N

355 - throw - assuming 60 deg dip, dip slip - throw, dip – assuming dip slip - throw, dip, rake –
356 assuming constant displacement orientation - direct off-set – with different permutations ...

357 4 Scan data Processing

358 I use point cloud spatial statistics to characterize and quantify active surface processes on faults.
359 I developed a *MatLab* work flow to entirely automate data processing from the raw *.xyz* input
360 format to the final statistical analysis:

361 1. Preprocessing

- 362 (a) manual inspection for coarsest defects
- 363 (b) Import *.xyz* data into *Matlab*
- 364 (c) Very coarse Height field filter
- 365 (d) Flatten points
- 366 (e) Grid data
- 367 (f) Orient grid along slip direction (using power spectral analysis)
- 368 (g) Remove defects
 - 369 i. Remove outliers in the height field
 - 370 ii. Fractal model filter
 - 371 iii. Remove abnormally flat (interpolated) sections

372 2. Processing

- 373 (a) Statistical analysis
 - 374 i. Scale dependent *RMS*
 - 375 ii. Scale dependent skewness
 - 376 iii. Scale dependent kurtosis
 - 377 iv. Scale dependent asymmetry
- 378 (b) Spectral Analysis
 - 379 i. Fast Fourier Transform (FFT)
 - 380 ii. Lomb-Scargle Periodogram

381 *make into figure, include bypasses and other recent additions*

382 Note that the general pre-processing workflow was slightly adapted according to the different
383 instruments that were used in the study. These adaptations were mostly attributable to the
384 quality of the data at the various scales of acquisition and the actual instrument specifications.
385 Scans collected with the LiDAR required more extensive manual point removal to avoid features
386 such as vegetation, spurious outliers and large defects to affect the quality of the preprocessing.
387 Scans collected at the intermediate scale with the laser scanner easily followed this workflow.
388 Finally, scans collected with the white light interferometer did require minimal preprocessing
389 and were aligned manually at the time of data collection.

390 4.1 Surface Pre-processing

391 Before conducting a statistical analysis scan data must be pre-processed into a workable format.
392 Scan data is a point cloud - a series of points with coordinates *x*, *y* and *z*. Scans reported in this
393 study typically have 10^6 to 10^7 points. In raw form, the point clouds are randomly oriented,
394 noisy and still contain instrumental and physical artefacts. Physical artefacts include cracks,
395 eroded sections, and vegetation; instrumental artefacts include noise, smoothing and scattering.
396 All these features must be removed. The process of manual removal is labour intensive and
397 unfeasible for a data set of the scope presented in this study. I rather opt to automate this
398 process. Only very large defects (defects that may substantially effect the quality of finding a
399 true mean plane) are manually removed.

400 4.1.1 Point Cloud orientation and Gridding

401 The surface must both be flattened and aligned along slip. Linear trends in the data induce an
402 unwanted high frequency signal in data and also affect the quality of later interpolation onto
403 a grid. Thus, x , y , z data is rotated using around the axis \mathbf{u} as determined by the normalized
404 cross product between the surface normal \mathbf{n} and a vector normal to a flat surface ($\mathbf{n}_2 = [001]$):

$$\mathbf{u} = \mathbf{n} \times \mathbf{n}_2 / |\mathbf{n} \times \mathbf{n}_2|$$

405 with the rotation,

$$R = \cos \theta \mathbf{I} + \sin \theta [\mathbf{u}]_x + (1 - \cos \theta) \mathbf{u} \otimes \mathbf{u},$$

406 were $[\mathbf{u}]_x$ is the cross product matrix of u and \otimes is the tensor product and I is the identity
407 matrix.

408 Fault surfaces are anisotropic. The direction of slip is preserved in the anisotropy whereby
409 the 'smoothest' direction is slip parallel and the 'roughnest' direction is perpendicular to slip.
410 The fault scan is rotated around the z axis such that the direction of slip is along the x axis.
411 The direction of slip is by decimating raw data before iteratd steps of regridding, one-degree
412 rotation and spectral analysis. In the radial search, roughness is quantified as the integral
413 of the log-weighted power spectrum over the entire bandwidth of the sample surface. The
414 angle associated to the minimum in roughness is then identified as the direction of slip and
415 subsequently used to rotated the original flattened point cloud. The data is then interpolated
416 onto a grid using a linear interpolation algorithm. The point spacing is automatically defined
417 by the point density over the areal extent of the data:

$$\Delta x = N_{pts} / AXXXXXX \quad (6)$$

418 4.1.2 Surface Defect Removal

419 INCLUDE HISTOGRAMS FOR EACH FILTER

420 *Defect* include all physical surface features that are clearly not associated any faulting
421 process, *e.g.* cracks, eroded patches, vegetation, etc.. Defects are idenetified and filtered out
422 using combination of thresholding methods. These methods all revolve around identifying clear
423 points or segments that are statistical outliers to the distribution characterizing the entire
424 surface—abnormal points.

425 The most aggressive filter implemented searches for outliers to the fractal model. The filter
426 removes entire linear segments with abnormally high variance in the height field for the given
427 scale of observation. For this implementation, I iterate over 10 filter scales. The scales are
428 selected using a log spacing from the 10 points up to the length of the entire surface. The
429 threshold for segment removal is chosen to be four standard deviations from the mean (should
430 account for < 0.1 percent of the data in a normal distribution). Note that, assuming a normal
431 distribution of variance data for a given scale, the filter should not induce a systematic bias since
432 the filtering is symmetric around the mean. However, surface features associated with a truly
433 distinct mechanism of formation, in this case cracks and other defects that will typically have
434 much higher variance, *are* be removed. This general approach ensures that defects, regardless
435 of their scale get identified and removed. This is important for any subsequent fractal analysis.

436 Abnormally flat sections arise as the result of triangular interpolation of sparse points.
437 Typically, interpolation on the edge on a non-convex set of points is subject to this effect.
438 These artefacts are readily identified in the curvature data. In the log-transformed absolute
439 value curvature field, these sections appear to be nearly or exactly zero. The filter rejects

440 point with curvatures less than 10^{-25} . These values likely associated to the linear interpolation
441 scheme.

442 Finally, all scan are inspected to make sure that the pre-processing was successful. The
443 script fails to properly process scans that are excessively populated with surface defects. These
444 scans were manually cleaned and oriented before re-processing them. Manual changes were
445 executed in *CloudCompare*.

446 Pre-processed scans are N by M scalar fields of fault surface topography(the sitance from
447 the mean plane) aligned with slip along the x axis. NaN values mark locations where data is
448 missing or was removed by filters. Point spacing is defined the mean point density of the scan
449 in the x - y plane.

450 4.2 Statistical Analysis

451 4.2.1 Spectral Analysis

452 After pre-processing, scans discretize defect-free slip surfaces with grids with rows aligned
453 with the slip direction. We compute the power spectral density content for every continuous
454 segment of every single profile of the grid using a Fast Fourier Transform (FFT). Individual
455 spectra are interpolated onto a master frequency vector. For a given frequency, the distribution
456 of power values across the profiles through along the slip is strongly skewed (see figure xxx).
457 The skewness is attributable to the non-negative constraint on power and residual outlying
458 profiles (defects not properly removed). To provide a more representative and robust measure
459 of maximum likelihood, we use the geometrical mean instead of the arithmetical mean. Ac-
460 cordingly, errors represent the 1σ range in the log-transformed distribution. The analysis yields
461 one representative spectrum for each scan.

462 In the spatial frequency content, fractal scaling is expressed as a power law. Extracting
463 fractal characteristic form Consistent with previous work (XXXXX), our scans for a given slip
464 surface display fixed scaling across out instrumental array (see figure XXX). The fixed scaling
465 provides means to remove instrumental artefacts. For our instruments, artefacts are particularly
466 disruptive at the small scale instrumental limit. The LiDar and laser scanner are dominated
467 by random noise, a shallower slope at the high frequency tail of the spectra. Conversely, the
468 spectra of the scan collected using the white light interferometer have steeper high frequency
469 tails. By comparing individual scan to a manually identified scaling across all our instrumental
470 scales of observation, we identify a conservatively defined bandwith overwhich the data is valid.
471 We reject data associated to affected frequencies for subsequent analysis.

472 We can further distill the roughness metric using the fractal model of the fault:

$$P(k) = Ck^{-\beta} \quad (7)$$

473 Accordingly the entire spectral information of a scan can be summarized with the prefac-
474 tor (C) and the scaling exponent (β). The fractal model is parametrized using a power law
475 regression through the spectra

476 4.2.2 More Spatial Statistics

477 INCLUDE A FIGURE WITH: ORIGINAL SURFACE, AUTOMATICALLY PROCESSED
478 GRID, MANUALLY PROCESSED GRID AND CORRESPONDING POWER SPECTRA.

479 identifying fractal scaling section plot of white light all magnifications computational scheme
480 to select the good section error on direct displacement estimates?

⁴⁸¹ **5 Results**

⁴⁸² **5.1 Observations**

Location	Lithology	Description	Displacement Constraints
Chimney Rock Fault Array	At the contact between the Navajo Sandstone and the base of the Carmel Unit	Orthorombic set of normal faults with preserved faults scarps of Navajo Sandstone	Displacement profiled of stratigraphic throw constrained by offset on a Carmel Limestone Marker Horizon by Maerten et al., 2000.
Big Hole Fault	Navajo Sandstone	One single large normal fault structure partitioning displacement on two major strands traceable for kilometers through a river wash with scarp exposure, and strike parallel/perpendicular cross-sectional exposure	Displacement constrained using the top Erosionally competent horizon at the top of the Navajo by Shipton and Cowie, 2003 and directly where possible.
Iron Wash	Navajo Sandstone	Network of normal and strike-slip cross-cutting faults. Little scarp exposure but has good cross-sectional exposure with fresh slip surfaces (using hammer and chisle)	Displacement mostly constrained by direct measurement of offset in the Upper Navajo horizon.
Molly's Castle	Entrada Sandstone	East-West striking network of normal faults and ubiquitous deformation bands. Well preserved slip surfaces broadly associated to a single slip surface structure intermittently bounding and crosscutting a thick (30 cm cluster of deformation bands	Displacement constraints available in places from mapping by Aydin (1978) and directly measured using various marker horizons within the Entrada Sandstone (e.g. laminae, cross-bedding unconformities, and thick red sandstone horizons depending on scale)

Table 1: Table caption

483

13

484

485 5.2 Field observations and Microstructure

486 The field observations and microstructures, in unison, build towards a qualitative characteri-
487 zation of fault maturation. I report on the fault architecture in the Navajo and Entrada Sand-
488 stones with a specific focus on the evolution from zero-displacement structures such as joints
489 and deformation bands to large offset structures with polished slip surfaces and accompanying
490 fault rock lithologies.

491 5.2.1 Fault architecture

492 Faults in the Navajo and Entrada sandstones generally record dip slip. Rotation of slip-direction
493 is typically associated points where larger fault structures crosscut each other. The general ar-
494 chitecture of the faults is complex. At all observable scales of observation, faults outcrop in
495 relays and cross-cutting conjugate sets typically dipping at 60° . The PSS fault model is only
496 rarely representative of the fault architecture. Fault zones rather have many slip surfaces,
497 sheared joints and splays which partition offset. As is characteristic for high porosity sand-
498 stone, fault zones all have deformation bands. The intensity of deformation bands decreases
499 exponentially away from the center of the fault zone and was shown to correlate in intensity
500 with displacement on the fault (cite someone). Deformation bands typically abut obliquely into
501 the slip surfaces at shallow angles (less than 70°). For an extensive review and description of
502 the faults in the Navajo and Entrada sand stones refer to Aydin's thesis.

503 1 or 2 : Photo j-; sketch of a cross-section through typical fault architectures

504 5.2.2 Zero-Displacement Structures

505 Deformations bands and joints are a ubiquitous and characteristic feature around faults in high
506 porosity sandstones. Larger fault structures nucleated from pre-existing networks of deforma-
507 tion bands and joints ([?]???). Deformation localizes and intensifies along theses structures to
508 then create through-going faults. The characteristics and surface morphology of these features
509 are especially relevant to our analysis as they represent the 'primordial roughness' of faults.

510 *Deformation bands* are recognizable in outcrop as sinuous white bands, 1 to 5 millimeters
511 in thickness, that accommodate shear offset. In sandstones, small strain can be mechanistically
512 accommodated by the run-away collapse of grains in sub planar sheets [?] ??. In thinsection,
513 ... The reduction of grain size and the associated compaction causes the deformation bands
514 to be stronger and more resistant to erosion than the host sandstone [?]. Unlike slip surfaces in
515 the area, deformation bands do not reduce the cohesion of the rock—they do not induce a well
516 define parting surface. Deformation bands preferentially resist erosion, often causing them to
517 protruded out of outcrops. *Deformation band clusters* accommodate more intense and localized
518 shear strain. The clusters are dense networks of anastamozing deformation bands ranging from
519 a few millimeters to tens of centimeters in thickness, often outcropping as slabs up to meters in
520 sizes (especially in the Entrada Sandstone). In the extensional regimes presented in this study,
521 clusters commonly form in upright conjugate pairs, each dipping 60° .

522 The edges of deformation band clusters that have eroded out appear to have a distinctly
523 corrugated and "lumpy" morphology (figure for this?). The orientation of the corrugations is
524 in clear agreement with cross-sutting slip surfaces kinematic indicators. The slabs are coated
525 with sand grains from the host sandstone. There is a clear directional asymmetry along the
526 direction of shear (see figure 1). Larger clusters often have one or many through going slip
527 surfaces. Cross cutting relationships along more mature fault structures show deformation
528 bands both pre-dating and postdating the nucleation of the fault. (*Probably need a figure for
529 this*). Please refer to Fossen, Shipton, Aydin for more detailed and extensive characterizations
530 of defomation bands in these localities.

531 Pre-existing regional joints sets are a common feature of every locality. Joints typically
532 have dips near 90° . Joints set are most readily measurable in the upper Navajo units and low
533 Carmel limestone pavements. The intensity of joint increases near the fault with the occurrence
534 of syn-kinematic sheared and splay joints. Refer to Aydin and Davatzes for extensive analysis
535 of joint characteristics and relative timing for each locality.

536 Systematic associations between the type and abundance of The Entrada unit is has more
537 deformation bands and fewer and less well defined joints. Moreover, in the Chimney Rock fault
538 array, there is a clear association to the conjugate fault set orientation. Faults striking



Figure 1: Left: Example of the edge of a deformation bands cluster at Molly's Castle. Note the "lumpy" morphology and an clear vertical directional asymmetry. Right: Cross-sectional view of a deformation band cluster with tens of centimeters of shear offset. It is unclear weather there is a through going slip surface localizing displacement. It is , however, definitely not on the edge of the cluster.

539 5.2.3 Slip Surfaces

540 Slip surfaces in the Navajo and Entrada sandstones are most readily identifiable by their vitreous
541 polish. Striations, grooves and mullions mark the direction of slip. In Cross-section slip surfaces
542 are sharp, smooth relative to their zero-displacement counterparts, and milky white with the
543 notable exception of the north fault in the chimney rock fault array, where well-preserved slip
544 surfaces had a distinct dark grey color. The slip surfaces often crosscut or bound deformation
545 band clusters. Slip perpendicular profiles are notably more sinuous than in the slip parallel
546 direction. Slip surfaces are only preserved in the Navajo and Entrada Sandstones. In spite of
547 good exposures in prospecting pits and careful inspection of the slip zone, the Navajo-Carmel
548 contact at the Chimney Rock fault array did not preserve good surfaces in the Carmel Unit.
549 It is unclear whether this indicates that the Carmel units is more susceptible to erosion and/or
550 alteration; or if a polished finish is only a feature of the quartzite sandstones. Pristine fault
551 slip surfaces are not cohesive, and always act as a parting surface. Slip surfaces uncovered *in*
552 *situ* using a hammer and chisel reveals a relatively consistent meso-scastructure (see figure –
553 figure similar to that in Jamies notes), A sharp interface, separated by a sub-mm thick layer of
554 incohesive white powder bounded by two vitreous surfaces is a dense set of deformation bands.

555 Surfaces that are notably more eroded and indurated have a reddish-brown to dark tarnish
556 and can loose their vitreous luster. Sections of the slip surface are plucked off. Severely
557 wethered scarps, not scanned in this study, develop a slip perpendicular fabric associated to
558 conjugate fractures and deformation bands abutting into the slip surfaces. We can confidently
559 attribute these effects to erosion because they did not occur in freshly parted slip surfaces and
560 appeared to have systematic association to sun exposure. Lichen grew preferentially on north
561 facing scarps. From our field observation, it is clear that erosion has the effect of re-roughening



Figure 2: Left: Example of at least two distinct polished slip surfaces on the same fault structure. Right: Example of concentric pattern on cross-sectional view a fault

562 the slip surfaces, especially at smaller scales. How the roughening process scales is, however,
563 unclear from our field observations.

564 In thin section...

565 Faults with small displacements on the order of millimeters to centimeters are distinctly
566 different than larger displacement faults. Smaller displacement faults are visibly more sinuous,
567 laterally discontinuous and less polished. They do not have well-defined gouge or cataclasites
568 layers bounding the slip surface. In spite of extensive investigation, we do not observe faults
569 with well-defined slip surfaces with clear offset markers indicating less than approximately half
570 a centimeter of displacement.

571 Microstructurally... (thin section + SEM pics)

572 5.2.4 Fault Rock

573 In this study, we refer to *fault rock* as rock altered either mechanically or chemically by the
574 influence of the fault. The faults in our study area display a very diverse range in fault rock
575 lithologies, ranging from fine-grained cataclasites to massive bodies of breccias (up to meters of
576 thickness). Fault rock consistently bounds slip surfaces—often asymmetrically. However, both
577 the lithology and thickness of the fault rock are highly heterogeneous and are subject to drastic
578 changes at the outcrop scale (10's of meters) both along the strike and dip. We pay careful
579 attention to the fault rock as it is inevitably coupled to the slip surface roughness and its
580 maturation with cumulative displacement.

581 Healed Gouges - the spot at big hole - iron wash (powder between the surface) - micro-
582 structure - prospecting pit - typically on thinned sections of the fault rock (near the slip
583 surface) Cataclasites . . . - big hole sample with slip surfaces on both sides of the cataclasite -
584 micro-structure - Breccias . . . - thick sections of the Breccias occur lenses which range from cm's
585 to meters in thickness. Breccia clasts are typically poorly sorted and can be very coarse with
586 clast up to 10 cm in diameter. Clasts show indications for multiple generations of brecciation.

587 Thin Quarts lens - iron wash

588 Systematic associations between fault rock and fault structure exist. For instance, Davatzes
589 et al., 2002 reports of a systematic association between the fault rock lithology and the ori-
590 entation of the fault set. Namely, the orthorhombic fault set striking WNW has systematic
591 association with fragmentation—fault breccias; conversely the ENE fault set rather has slip sur-
592 faces cutting through deformation band clusters (see figure ??). This relation was speculated to
593 be the result of contrasting genetic mechanism. The WNW set is the result of the reactivation
594 of regional joints. In contrast the ENE fault set is the the result of clustering and anastamosing
595 deformation bands acting as a catalysing agent to the formation of a faults. In this study, we

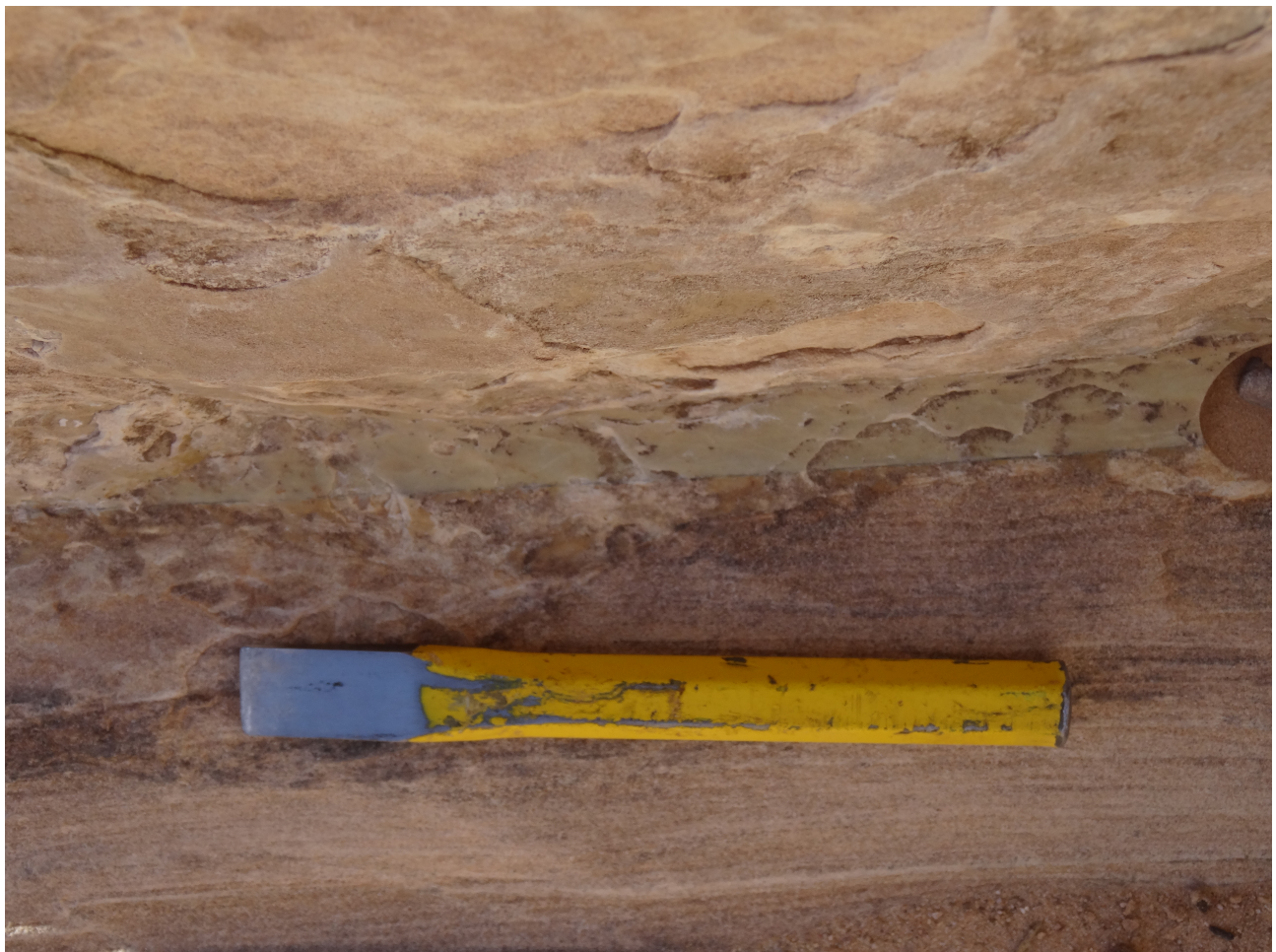


Figure 3: Example of a slip surface interpreted as a principle slip surface with around 20 meters of displacement at Big Hole Fault

596 observe clear instance of lithological contacts being associated to brecciation (photo at iron
597 wash where the top of the Navajo is brecciated and quickly reverts to a single fault strand.
598 More over, large breccia bodies are clearly related to points where faults are cross-cutting each
599 other at high obliquity as is often the case at the Chimney Rock fault array and

600 Complicating factors:

601 Associations between brecciation and lithological contacts...

602 Associations between brecciation and cross cutting faults...

603 5.3 Roughness measurements

604 figures to include:

- 605 • all spectra
606 • increasing anisotropy (two surfaces) - polar plot

607 Figure XXX shows the all the PSD calculations obtained from the scans collected in
608 this study. Consistent with previous work, we find that the PSD spectra over the entire
609 bandwidth reported in this study generally follow a linear relation in log-log space. This
610 feature corresponds to the constant fractal scaling. The scaling exponent and pre-factors
611 are calculated based on the slop of a linear least-squares fit of the spectra in log-log space.
612 The Hurst exponent can then be obtained according to equation XXX.

613 In the slip perpendicular direction, Hurst exponents range from XXX to XXX, with an
614 average value of 0.8ish; Prefactors range from XXX to XXX with an average value of
615 XXX. In the slip parallel direction, Hurst exponents range from XXX to XXX, with an
616 average value of 0.8ish; Prefactors range from XXX to XXX with an average value of
617 XXX. Implicit to the pre-processing grid alignment, for any single scan the slip parallel
618 direction is systematically smoother than the slip perpendicular direction indicating a
619 clear surface anisotropy. The entire data set does however indicate an overlapping range
620 in slip parallel and perpendicular directions. We also note that lower pre-factors are
621 generally associated to lower Hurst exponents.

622 An evolution with displacement is weakly expressed in the spectral analysis but is cluttered
623 and obscured by highly variable errors on displacements and roughness measurements.
624 In order to highlight the effect of displacement on the surface roughness, we separate our
625 scan data into two distinct populations. 1) Scan data with direct displacement constraint
626 and 2) scan data associated to maximum displacement constrains. Brodsky et
627 al., 2011, tested the validity of a power law relation between fault roughness are various
628 specific scales and displacement. Building upon this approach, we use both data populations
629 to test the validity and parameterization of the fit and the Implicit hypothesis that
630 faults smooth as a function of displacement—the smoothing model. Scan data with direct
631 displacement constraints serves as a direct test and a means to parametrize the smoothing
632 model. For the model to be valid it must agree with further constraints imposed by data
633 with only maximum displacement estimates.

634 A point defined by the maximum error bound on displacement and the roughness of
635 the fault surface is in agreement with smoothing model if it is rougher than roughness
636 prescribed by the model as parametrized by direct measurement. Conversely, if the point
637 is rougher than the model prediction, it is not physically possible in the model construct.
638 A null hypothesis would prescribe no bound on the roughness and would simply have
639 the predicted roughness of a fault be defined by the probability distribution function of
640 the entire roughness dataset. Accordingly, we can roughly estimate the probability that

641 our distribution of data relative to the smoothing model is a random element of chance
642 according to:

$$P = \prod p(y_i > Y(x_i)) \quad (8)$$

643 Figures XXX to XXX shows the relation between roughness and displacement as interpo-
644 lated a various scales of observation. Vertical error bars on the power spectral density are
645 obtained from the confidence interval of the of the fractal model regression. Horizontal
646 errorbars on displacement are defined on a case by case basis from field observations and
647 previous work in on the fault arrays. We present both the fit through the our entire dataset
648 (comprised of direct and upper bound constraints on displacement) and through the the
649 directly constrained displacement estimates. Fits are obtained using a least squares linear
650 regression through the log-transformed data sets. In order to provide error bounds on
651 the fit parameters, we use a full Monte Carlo simulation sampling direct displacement
652 estimated as Gaussian distributions, upper bound displacement constrains as completely
653 random distributions across the entire possible range of displacements and power spectral
654 density estimates as log normal distributions. Errors represent on standard deviation
655 estimated from 10000 simulations.

656 The weak trend across the entire dataset imply and expectation of smoother slip surfaces
657 in fault zones which have accommodated larger displacement.

658 Conversely the stronger trend across the well constrained data implies that an individual
659 slip surface smooths with displacement. The smoothing exponent varies according to
660 the different scales of observation (XXX at the laser at the centimeter scale, XXX at
661 the milimeter scale and XXX at the micron scale). While a power law fit to the best
662 constrained measurements is has poor fit metrics, we find a nearly perfect agreement
663 with roughness measurements only associated to upper bound constraints.

664 Two constraints on displacement – two data populations plot of all the spectra color coded
665 with displacement smoothing plots: parallel - ζ all scales perpendicular - ζ all scales Hurst
666 exponent - ζ all scales Fit for smoothing through direct data, discuss consistency with
667 max disp data Other statistical metrics? Poly-gaussian features in the surface roughness
668 Skewness of height field as a function of scale Null result worth reporting? Do a plot of
669 the evolution of skewness at the grain scale?

670 5.3.1 Lidar

671 qualitative illustration of maturity

672 5.3.2 Laser scanner

673 5.3.3 White light

674 6 Interpretation of field observations and roughness 675 measurements

676 6.1 Hard facts

677 The following is a list of ‘hard facts’ that can be established from the both the qualitative
678 and quantitative data:

- faults are smoother than joints or deformation bands
 - * power spectrum shows that fault slip surfaces are systematically smoother than joint and deformation band surfaces at all wave lengths reported in this study (10^{-6} to 10^5 meters)
- At the grains scale, grains are truncated, not ‘plucked’.
- The roughness of a slip surface is sensitive to its displacement history. This result is robust across multiple faults both nucleated from deformation bands and joints and variations in fault rock and host rock lithology.
- The smoothing exponent is likely more than 1 at certain scales - quote from Emily: “In all of these cases, the scatter of the data is large, but the basic result holds: the absolute value of the exponent is much less than 1.”
- The smoothing rate is highest at small displacements and decreases with displacement.
- Smoothing occurs at all scales of this study
- a slip surface from a large offset fault is more likely to be smoother
- for any given the displacement on a fault, the smoothest slip surface roughly follows the same smoothing trend as that defined by direct displacement measurements.
- The roughness varies spatially on a slip surface - the scatter in the data exceeds the instrumental error
- the height distribution of points on a slip surface can be far from normally distributed.
- the Hurst exponent has a very large range in values (less than Zero to 0.9)
- more linear fault traces where not offset by wavier fault traces

7 Model

7.1 Modelling Objectives

7.2 Model Outline

In this study, we utilize work minimization numerical modelling to capture the growth of fault damage and the effect of rough asperities. The models are built off of fric2d and growth by optimization of work (GROW) developed by Michele Cooke and Jessica McBeck.

7.2.1 GROW

Growth by optimization of work predicts fracture propagation paths. It does so by minimizing the external work on the system. The model theoretically allows for the simultaneous growth of multiple fractures and

The general algorithm uses a boundary element method to describe the fractures–linear dislocation elements that discretize the entire length of the fault. As a crack grows, dislocation elements are added radially to the tip of the crack so as to minimize the external work on the system normalized by the crack area ($W_{ext}/\Delta A$). External work is further defined as:

$$W_{ext} = \oint (\tau u_s + \sigma_n u_n) dB \quad (9)$$

718

7.3 Model Results

719

8 Discussion

720

8.0.1 Tying the model together with roughness measurements and model

721 wear rate (character), tying together model with

722

8.1 An external estimate of gouge production and fault thick-

723 ness

724 The data collected in this study offers the unique opportunity to provide new indirect
725 estimates of fault rock production, fault thickness and dilation rate over an entire fault.
726 We know that 1) the primordial roughness is systematically rougher than mature faults,
727 2) the primordial roughnes is relatively constant, and 3) the roughness can be estimated
728 for a given displacement. Using these results, I will estimate the volume of fault rock
729 produced through wear and the corresponding roughness induced accomodation space in
730 the fault system.

731 Displacing two rough fractal surface in shear requires dilation. The expectation dilation
732 can be estimated according to the amplitude of the largest wavelength (λ) being offset
733 (see figure XXX). For a given displacement, u , the largest wavelength in the system
734 will be $\lambda = 2u_i$. Using a fractal paradigm to define the average amplitude of a given
735 wavelength according to the pre-factor β and the Hurst scaling exponent, H , (*reference
736 the equation*) we find that the dilation, A can be expressed as a function of displacement:

$$A(u) = \sqrt{\beta 2u^{-2H-1}} \quad (10)$$

737 If we apply this to an entire fault system with displacement field, U , we can estimate the
738 void space that would be produced:

$$V_{void}(U) = \int_S \sqrt{\beta 2U^{-2H-1}} dS \quad (11)$$

739 Since the fault system is closed any change in fault roughness *must* be coupled to the fault
740 core. If all changes in the fault surface are associated to a production of fault rock, we can
741 effectively estimate the volume of fault rock that has been produced from diplacement
742 u_0 to u_f by comparing the volume integral under the corresponding initial and final slip
743 surfaces $S(u_0)$ and $S(u_f)$.

$$\frac{\Delta V_{faultrock}}{\Delta u} = \int_S S(u_0) - S(u_f) dS \quad (12)$$

744 volume integral under the surfaces, S , can be estimated numerically according to the
745 frequency distribution prescribed by the RMS the entire fault system. Note that the
746 RMS is estimated at the length scale of the entire fault; wear processes are active at all
747 length scales below this.

$$\int S dS \approx \quad (13)$$

Now for the displacement field, U , we can estimate the total fault rock produced by using the primordial surface roughness, $S(0)$, and the prediction of the surface roughness extrapolated to the length of the fault (* reference the the equation of smoothing *) such that:

$$V_{faultrock}(U) = \int_S S(0) - S(U) dS \quad (14)$$

The comparison between the two quatities is telling. If the amount of fault rock is

9 conclusion

9.1 future work

10 Appendix

10.1 Surface Processing scripts

Or possibly a link to a git repository...

10.2 User manual for script

This manual should serve as both a basic guide to the logic and usage of the *surface processing package*.

The master function of the package is *surfaceprocessing*. This function effectively deal with the inputs and direct computations towards the necessary functions. Outputs of the function are a .mat workspace file for each input data file. The workspace includes a structure (called *parameters*) with the raw surface analysis outputs, the point spacing, the decimation factor (if any), the file name and the date of the analysis. The workspace also includes the grid form of the original inputed surface (called *surface*), and the pre-processed copy that was used for the subsequent analysis (called *zGrid*). Inputs are always included in pairs. The former defines the type of input, the latter qualifies or quantifies the input. This structure allows for adaptability of the code to various needs. Options include the following:

- *what to do?*: ‘*toDo*’, followed by the desired analyses on of: ‘FFT’, ‘PLOMB’, ‘parameters’ or ‘all’ (default is ‘all’) - can be a cell array. This specifies what kind of spatial analysis will be done on the input surface data. The spatial analysis is calculated and averaged across every single profiles along the surface. The analyses are the following:
 - * ‘FFT’, a power spectrum computed using a Fast Fourier Transform (FFT) algorithm;
 - * ‘PLOMB’, a power spectrum computed using a least-squares Lomb-Scargle algorithm;
 - * ‘paramters’, the calculation (as a function of scale) of the Root Mean Squared (RMS), skewness, kurtosis and asymmetry averaged across all segments of a given length on all profiles of the surface.

- 783 'all' simply performs all the analyses outlined above.
- 784 – *skip pre-processing?*: 'bypass', followed by 'zygo', 'pre-processing' or 'no' to be used
 785 input is already in aligned clean grid form - input files are then (default is 'no').
 786 'zygo' is specifically adapted to the proprietary data format of the white light in
 787 Wong. 'pre-processing' simply skips any pre-processing. This option requires a
 788 .mat structure with a field named 'grid' with the topography and a field name
 789 'pointSpacing' specifying the point spacing (in meters). In either case the topography
 790 must be aligned such that the positive x direction is the parallel direction.
- 791 – *for the parameter analysis, how many scales?* 'numberOfScales' followed by the
 792 desired number of analysed scales. This option is relevant to the parameters analysis.
 793 Note that this has a lot of effect on the amount of processing time (default is 10).
- 794 – *decimation*: 'decimationFactor' followed by the desired decimation factor (default is
 795 1). Decimation is a useful tool to reduce computation time. The surface grid is sub-
 796 sampled according to the decimation such that a decimation factor of k would imply
 797 that only every k th point on the every k th will be considered for hte subsequent
 798 analysis.
- 799 – *Instrument specific analysis* 'instrument' followed by 'white light', 'laser scanner' or
 800 'lidar' (default does not set any instrument specific adjustments). Some instrument
 801 specific pre-processing steps are taken. Please contact me if you intend to use this
 802 as they may be highly dependent on the specific instrument used.

803 For instance, `surfaceprocessing('todo','FFT','bypass','zygo')` will only perform a power
 804 spectral density analysis and will skip preprocessing and assume that all input will be in
 805 the 'zygo' export .xyz format.

806 When the command is executed, the user will be prompted to navigate to the directory
 807 where the input data is located. IMPORTANT: the directory must *only* contain files of
 808 one data format. There cannot be other files or sub-directories in the directory. The user
 809 will then be prompted to choose a destination for the output data. The requirements
 810 for the output location are less stringent. However, it is advisable to choose an empty
 811 directory such as to facilitate subsequent steps.

812 The next step is to visualize the output of the analysis. This is done using the *unpack*
 813 parameters function. This function provides various visualization options for all files in
 814 the directory chosen by the user. The first input (the *desired plot*) can be one of the
 815 following:

- 816 'FFT': plot all power spectra;
- 817 'PLOMB': periodogram plot as determined by the Lomb-Scargle least squares anal-
 ysis;
- 819 'topostd': plot of the root mean squared (RMS) as a function of scale;
- 820 'topoSkew': plot of skewness of height fields as a function of segment scale;
- 821 'topoKurt': plot of the the kurtoisis of height fields as a function of segment scale;
- 822 'PowerVsDisp': plot of power interpolated at a given scale as a function of displace-
 ment;
- 824 'RMSVsDisp': model RMS at a given scale as a function of displacement
- 825 'Grids': shows both the original and pre-processed grid for the specified file 'file-
 Name';

827 *'Best Fits'*: best logarithmic fits to power spectra obtained from the fast fourier
828 transform analysis.

829 The functionality of the packages is broadly divided into three sections: 1) importing and
830 preprocessing data, 2) performing various spatial statistics on the pre-processed data, and
831 3) unpacking the analysis output into figures.

832 In order to run smoothly the all functions included in the package should be kept in the
833 same directory or on an accessible path.

834 For reference, here is a quick outline of what each function does:

835 *affine'fit*: (from mathworks) Computes the plane of best fit using least squares
836 normal distance;

837 *align'grid*: finds the smoothest directions in a grid using FFT spectra and rotates
838 and re-grids the input grid;

839 *fault'spectral'density'simple*: Calculates the average lomb-scargle spectral density
840 every row of a N by M array;

841 *FindErr'loop'anisotropy*

842 *flatten'XYZ*: removes planar trends from XYZ data by applying a rotations matrix
843 according to the best fit plane (*affine'fit*);

844 *fractal'model'outlier*: Removes outlying segments according to a near-gaussian model
845 for the distribution of RMS values at specified segment lengths (or scales);

846 *frequency'spectrum*: Calculates the average lomb-scargle spectral density of all con-
847 tinuous segments on every single row of a N by M array;

848 *parse'zygo'format*: extracts the both the point spacing and topographic grid from
849 the exported zygo format. Can also remove planar trend from data (substracted
850 from grid);

851 *rotateZ*: applies rotation matrix on XYZ data

852 *surface'analysis*: Aggregates the analysis functions and applies them to an input
853 grid

854 *surface'cleaning*: removes outliers associated to surface defects

855 *surface'parameters*: calculates spatial statistics and parameters along segments as a
856 function of scale (RMS, skewness, directional asymmetry and kurtosis)

857 *surface'preprocessing'2*: deals with preprocessing input data (import data, cleaning
858 and gridding data)